

# QSO 0347-383 and the invariance of $m_p/m_e$ in the course of cosmic time <sup>★</sup>

M. Wendt<sup>1</sup> and P. Molaro<sup>2</sup>

<sup>1</sup> Institut für Physik und Astronomie, Universität Potsdam, 14476 Golm, Germany  
 e-mail: mwendt@astro.physik.uni-potsdam.de

<sup>2</sup> Osservatorio Astronomico di Trieste, Via G. B. Tiepolo 11, 34131 Trieste, Italy

Received March 26, 2022; accepted – –

## ABSTRACT

**Context.** The variation of the dimensionless fundamental physical constant  $\mu = m_p/m_e$  – the proton to electron mass ratio – can be constrained via observation of Lyman and Werner lines of molecular hydrogen in the spectra of damped Lyman alpha systems (DLAs) in the line of sight to distant QSOs.

**Aims.** Our intention is to max out the possible precision of quasar absorption spectroscopy with regard to the investigation of the variation of the proton-to-electron mass-ratio  $\mu$ . The demand for precision requires an understanding of the errors involved and effective techniques to handle present systematic errors.

**Methods.** An analysis based on UVES high resolution data sets of QSO 0347-383 and its DLA is put forward and new approaches to some of the steps involved in the data analysis are introduced. We apply corrections for the observed offsets between discrete spectra and for the first time we find indications for inter-order distortions.

**Results.** Drawing on VLT-UVES observations of QSO 0347-383 in 2009 our analysis yields  $\Delta\mu/\mu = (4.3 \pm 7.2) \times 10^{-6}$  at  $z_{\text{abs}} = 3.025$ .

**Conclusions.** Current analyzes tend to underestimate the impact of systematic errors. Based on the scatter of the measured redshifts and the corresponding low significance of the redshift-sensitivity correlation we estimate the limit of accuracy of line position measurements to  $\sim 220 \text{ m s}^{-1}$ , consisting of roughly  $150 \text{ m s}^{-1}$  due to the uncertainty of the absorption line fit and about  $150 \text{ m s}^{-1}$  allocated to systematics related to instrumentation and calibration.

**Key words.** Cosmology: observations – quasars: absorption lines – quasars: individual: QSO 0347-383

## 1. Introduction

The Standard Model of particle physics contains several fundamental constants whose values cannot be predicted by theory and need to be measured through experiments (Fritzsche 2009). They are the mass of the elementary particles and the dimensionless coupling constants which are assumed time-invariant although in theoretical models which seek to unify the four forces of nature they vary naturally on cosmological scales. The fine-structure constant  $\alpha \equiv e^2/(4\pi\epsilon_0\hbar c)$  and the proton-to-electron mass ratio,  $\mu = m_p/m_e$  are two constants that can be probed in the laboratory as well as in the Universe by means of observations of absorption lines due to intervening systems in the spectra of distant QSOs and have been the subject of numerous studies. The former is related to the electromagnetic force while the latter is sensitive primarily to the quantum chromodynamic scale (see, i.e., Flambaum 2004).

A probe of the variation of  $\mu$  could be obtained by comparing relative frequencies of the electro-vibro-rotational lines of  $\text{H}_2$  as first applied by Varshalovich and Levshakov (1993) after Thompson (1975) proposed the general approach to utilize molecule transitions for  $\mu$ -determination. The original paper by Thompson (1975) did not take into account the different sensitivities within the molecular bands, which is the key of the modern approach.

The method is based on the fact that the wavelengths of vibro-rotational lines of molecules depend on the reduced mass,

$M$ , of the molecule. For molecular hydrogen  $M = m_p/2$  so that the comparison of an observed vibro-rotational spectrum with its present analog will give information on the variation of  $m_p$  and  $m_e$ . Comparing electro-vibro-rotational lines with different sensitivity coefficients gives a measurement of  $\mu$ .

The observed wavelength  $\lambda_{\text{obs},i}$  of any given line in an absorption system at the redshift  $z$  differs from the local rest-frame wavelength  $\lambda_{0,i}$  of the same line in the laboratory according to the relation

$$\lambda_{\text{obs},i} = \lambda_{0,i}(1+z)(1 + K_i \frac{\Delta\mu}{\mu}), \quad (1)$$

where  $K_i$  is the sensitivity coefficient of the  $i$ th component computed theoretically for the Lyman and Werner bands of the  $\text{H}_2$  molecule (Varshalovich & Levshakov 1993, Varshalovich & Potekhin 1995, Potekhin et al. 1998, Meshkov et al. 2007, Ubachs et al. 2007).

It is useful to measure variations in velocities with comparison to the redshift of a given system defined by the redshift position of the lines with  $K_i \approx 0$ , then introducing the reduced redshift  $\zeta_i$ :

$$\frac{\Delta V_i}{c} \approx \zeta_i \equiv \frac{z_i - z}{1+z} = K_i \frac{\Delta\mu}{\mu}. \quad (2)$$

The velocity shifts of the lines are linearly proportional to  $\Delta\mu/\mu$  which can be measured through a regression analysis in the  $\Delta V_i - K_i$  plane.

This method was used to obtain a bound on the secular variation of the electron-to-proton mass ratio at  $\Delta\mu/\mu = (-1.8 \pm$

<sup>★</sup> Based on observations taken at ESO Paranal Observatory, Program 083.A.0733

$3.8) \times 10^{-5}$  from observations of the newly discovered  $H_2$  absorption systems at  $z_{abs} = 3.0$  towards QSO 0347-383 (Levshakov et al. 2002). Subsequent measures of the absorption systems of QSO 0347-383 and QSO 1232+082 provided a strong indication of a variation  $(2.4 \pm 0.6) \times 10^{-5}$ , i.e. at  $3.5 \sigma$  (Reinhold et al. 2006, Ubachs et al. 2007). Earlier works (Ivanchik et al. 2005) also find hints for variation, but are still dominated by inaccuracies of the laboratory wavelengths. However, more recently King et al. (2008), Wendt & Reimers (2008), Thompson et al. (2009a), Wendt and Molaro (2011), King et al. (2011) with  $\Delta\mu/\mu = (0.3 \pm 3.7) \times 10^{-6}$  at  $z_{abs} = 2.811$  towards PKS 0528-250 and Bagdonaitė et al. (2012) with  $\Delta\mu/\mu = (-6.8 \pm 27.8) \times 10^{-6}$  at  $z_{abs} = 2.426$  towards QSO 2348-011 reported a result in agreement with no variation.

The more stringent limits on  $\Delta\mu/\mu$  have been found from the combination of three  $H_2$  systems at  $\Delta\mu/\mu = (2.6 \pm 3.0_{stat}) \times 10^{-6}$  (King et al. 2008) and taking into account additional transitions from deuterated molecular hydrogen (HD) in King et al. (2011). A fourth system has provided  $\Delta\mu/\mu = (+5.6 \pm 5.5_{stat} \pm 2.9_{sys}) \times 10^{-6}$  (Malec et al. 2010).

An independent method relies on the inverse spectrum of ammonia as shown by Flambaum & Kozlov (2007). Ammonia  $NH_3$  inversion transitions are very sensitive to changes in  $\mu$  due to a tunneling effect. The sensitivity coefficient of the inversion transition can be almost two orders of magnitude more sensitive to  $\mu$ -variation than  $H_2$  molecular rotational frequencies. Thus by comparing the inversion frequency of  $NH_3(1,1)$  with a rotational frequency of another co-spatial molecule it is possible to bind a variation of  $\mu$ .

Flambaum & Kozlov (2007) combine three detected  $NH_3$  absorption spectra from B0218+357 with rotational spectra of CO,  $HCO^+$ , and HCN to place a limit of  $(0.6 \pm 1.9) \times 10^{-6}$  for a look-back time of 6 Gyr (redshift  $z = 0.68$ ). Murphy et al. (2008) with newly obtained high signal-to-noise rotational spectra of  $HCO^+$  and HCN obtained  $< 1.8 \times 10^{-6}$  at a 95% CL.

Henkel et al. (2009) obtained a firm upper limit of  $10^{-6}$  for a look-back time of 7 Gyr ( $z = 0.89$ ) towards PKS 1830-211. This method is limited to low redshifts due to the small number of  $NH_3$  sources in general and to the large line widths and chemical segregation of different molecules at higher redshifts. For sources in the local Milky Way, however, a very strict upper limit of  $|\Delta\mu/\mu| < 3 \times 10^{-8}$  was found utilizing both the ammonia method (Levshakov et al. 2010a, and Levshakov et al. 2010b), and the methanol method (Levshakov et al. 2011).

Laboratory experiments by comparing the rates between clocks based on hyperfine transitions in atoms with a different dependence on  $\mu$  restrict the time-dependence of  $\mu$  at the level of  $(\dot{\mu}/\mu)_0 = (1.6 \pm 1.7) \times 10^{-15} \text{ yr}^{-1}$  (Blatt et al. 2008).

In the following we will concentrate on the  $H_2$  system observed towards QSO 0347-383 to trace the proton-to-electron mass ratio  $\mu$  at high redshift ( $z_{abs} = 3.025$ ). The motivation for re-analysis of QSO 0347-383 is given by the dramatically enhanced quality of the recent data of this quasar for the purpose of setting constraints on  $\Delta\mu/\mu$ . The single velocity component in  $H_2$  absorption renders QSO 347-383 a prime target to further investigate the impact of wavelength calibration issues. Trying to reach a sensitivity of few parts per million everything becomes important and the special requirements of the observations as described in the following section are absolutely mandatory.

## 2. Data

### 2.1. Observations

The recent observations of QSO 0347-383 were performed with UVES on VLT on the nights of September 20-24 2009. The journal of these observations is given in Table 1. The DIC 2 setting was used with blue setting and the 437 nm grating. The CCDs were not binned with pixel size of  $0.013 - 0.015 \text{ \AA}$ , or  $1.12 \text{ km s}^{-1}$  at 400 nm along the dispersion direction. The observations are comprised of 11 exposures on four successive nights, of which 10 exposures were of 5400 s and one of 3812 s. Eight of the spectra with setting 437+760 and three the 437+860 setting, providing a coverage in the blue spectral ranges between 373-500 nm. QSO 0347-383 has no flux below 370 nm due to the Lyman discontinuity of the  $z_{abs} = 3.023$  absorption system. The slit width was set to  $0.7''$  for all observations providing a

**Table 1.** Journal of the observations (2009 data). Before and after each spectrum, a 30 s calibration frame was recorded

No.	Date	Time	$\lambda$	Exp[s]	DIMM[arcsec]
1	2009-09-20	05:05:46	437	5400	1.21(0.29)
2	2009-09-20	08:28:48	437	3812	1.73(0.23)
3	2009-09-21	04:45:51	437	5400	1.15(0.12)
4	2009-09-21	06:18:45	437	5400	1.21(0.18)
5	2009-09-21	07:59:24	437	5400	1.08(0.09)
6	2009-09-22	04:41:37	437	5400	0.97(0.17)
7	2009-09-22	06:14:25	437	5400	1.03(0.13)
8	2009-09-22	07:59:19	437	5400	1.00(0.14)
9	2009-09-23	04:24:05	437	5400	1.36(0.26)
10	2009-09-23	05:56:49	437	5400	1.18(0.23)
11	2009-09-23	07:29:35	437	5400	0.95(0.23)

mean resolving power of  $\lambda/\Delta\lambda \approx 66000$ . Within each order the resolving power varies by about 15-20 % being higher at the starting wavelength of each order. The average seeing along the exposures as recorded by the DIMM at Paranal is given in the last column of Table 1. We note, however, that the actual seeing at the UT2 of VLT was significantly better than that recorded by the DIMM.

The 11 different spectra and the corresponding co-added data (*bottom*) are shown in a region around L4R1 in Figure 1.

### 2.2. Reduction

The last version of the UVES pipeline<sup>1</sup> has been used for data reduction. The pipeline first uses a set of five bias to make a mean bias free of cosmic ray hits which is then subtracted to all the two dimensional format images. A pinhole lamp image is used for identifying the precise location of the Echelle orders which are curved and tilted upwards.

The pixel-wavelength conversion of the wavelength calibration is done by using the corresponding calibration spectrum. Murphy et al. (2008) and Thompson et al. (2009) independently showed that the standard Th/Ar line list used in the old UVES pipeline was a primary limiting factor. The laboratory wavelengths of the calibration spectrum were only given to three decimal digits (in units of  $\text{\AA}$ ) and, in many cases, the wavelengths were truncated rather than rounded from four decimal places (see Murphy et al. 2007).

<sup>1</sup> Version 4.9.5

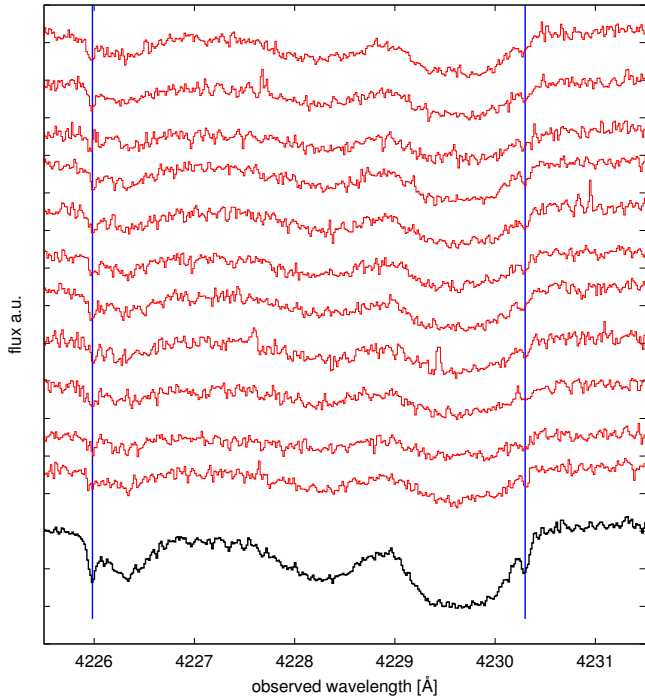


**Fig. 1.** The 11 single spectra and the corresponding co-added data (*bottom*) are plotted around the region of L4R1 and L4P1 (*vertical lines*). The stronger  $H_2$  features can be merely distinguished in single spectra.

Thompson et al. (2009) re-calibrated the wavelength solutions using the calibration line spectra taken during the observations of the QSOs and argued that the new wavelength calibration was a key element in their null result.

The new data UVES pipeline has solved these problems.

The UVES blue frame comprise 32 orders, from absolute number 96 to 124, covering the wavelength range 374-497 nm while the molecular lines are spread over 18 UVES echelle orders (from 106-122) covering the wavelength range 380-440 nm.

More than 55% of the  $\approx 400$  ThAr lines in the region were used to calibrate the lamp exposure by means of a polynomial of the 5th order. Typical residuals of the wavelength calibrations were of  $\sim 0.34$  mÅ or  $\sim 24$  m s $^{-1}$  at 400 nm and were found symmetrically distributed around the final wavelength solution at all wavelengths. By comparison in Malec et al. (2010) the wavelength calibration residuals have been RMS  $\sim 80$  m s $^{-1}$ .

In our set of observations, calibration spectra were taken before and after the object spectra for each night. Calibration lamps taken immediately before and after object observation provides accurate monitoring of physical variations. Moreover, the calibration frames were taken in special mode to avoid automatic spectrograph resetting at the start of every exposure. Since Dec 2001 UVES has implemented an automatic resetting of the Cross Disperser encoder positions at the start of each exposure. This implementation has been done to have the possibility to use daytime ThAr calibration frames for saving night time. If this is excellent for standard observations, it is a problem for the measurement of fundamental constants which requires the best possible wavelength calibration. Only calibration spectra that are *attached* as template to the OB allow to take the calibration exposure in exactly the same instrument setting as the science exposure. These calibrations can be taken upon user's request in addition to the ones from the calibration plan. Thermal-pressure changes move in the cross dispersers in different ways, thus in-

roducing relative shifts between the different spectral ranges in different exposures.

It should be emphasized that this effect has not been taken into account in the analysis performed so far on UVES data for  $\mu$  variability.

There are no measurable temperature changes for the short exposures of the calibration lamps but during the much longer science exposures the temperature drifts generally by 0.1 K, and in two cases the drift is of 0.2 K while in other two there is no measurable change. Pressure values are surveyed at the beginning and end of the exposures and changes range from 0.2 to 0.8 mbar. The estimates for UVES are of 50 m s $^{-1}$  for  $\Delta T = 0.3$  K or a  $\Delta P = 1$  mbar (Kaufer et al. 2004), thus assuring a radial velocity stability within  $\sim 50$  m s $^{-1}$ .

Individual spectra are corrected for the motion of the observatory about the barycenter of the Earth-Sun system and then reduced to vacuum. The velocity component along the direction to the object of the barycentric velocity of the observatory was calculated using the date and time of the midpoint of the integration to minimize the influence of changes. The changes in radial velocity during exposure induce a symmetric modification of the line profile. The absorption profile is not strictly Gaussian (or Voigt) anymore but rather slightly squared-shaped (since the FWHM of the line is  $\approx 5$  km s $^{-1}$  and the smearing of the line by Earth motions of  $\pm 40$  m s $^{-1}$  the effect is negligible. The line shapes remain symmetric in any case and possible changes of radial velocities during exposure effects only the quality of the fit, it does not influence the measured centroid of an absorption line. The wavelength scale was then corrected for this motion so that the final wavelengths are vacuum wavelengths as observed in a reference frame at rest relative to the barycenter.

The air wavelengths have been transformed into vacuum by means of the dispersion formula by Edlen (1966). Drifts in the refractive index of air inside the spectrograph between the ThAr and quasar exposures will therefore cause miscalibrations. According to the Edlen formula for the refractive index of air, temperature and atmospheric pressure changes of 1 K and 1 mbar would cause differential velocity shifts between 370 nm and 440 nm of  $\sim 10$  m s $^{-1}$ .

### 3. Preprocessing

#### 3.1. Spectral radial velocity shifts

Wendt and Molaro (2011) showed the presence of overall shifts between spectra obtained with slit spectrographs such as UVES. For checking such a possibility in the new data set we obtained a median velocity per each exposure by fitting as many lines as possible in each of the eleven spectra. The 50  $H_2$  lines were initially selected for that, but due to the relatively low SN spectra in single exposures, not all could be fitted, and for instance most of the weak  $J=0$  transitions have been missed. The median radial velocity in respect to the chosen absorber redshift derived from all detected lines within an individual exposure ranges from -200 m s $^{-1}$  to +354 m s $^{-1}$  for the 11 spectra. Due to the low quality of the fits to single lines of individual spectra with low signal-to-noise, the median was chosen. Despite the low quality of the individual fits the median velocities listed in Table 2 are well defined as shown in Figure 2. Bootstrapping is a useful practice of estimating properties of an estimator (i.e. its error). For example 48 line positions were determined in spectrum 8 (see Table 2). Their median velocity offset corresponds to 310 m s $^{-1}$ . The bootstrap histograms were implemented by constructing a number of resamples of the observed line positions (and of equal size

**Table 2.** Median velocities of single spectra

spectrum	median velocity [km s <sup>-1</sup> ]	lines considered
1	0.075	46
2	0.058	42
3	-0.136	41
4	0.223	43
5	0.354	47
6	-0.206	47
7	-0.015	44
8	0.310	48
9	-0.051	40
10	-0.107	47
11	-0.004	48
	0.046	

to the observed data set), each of which is obtained by random sampling with replacement from the original data set.

For the data at hand the obtained velocity offsets bear no statistical significance because of the large scatter of the individual position measurements per single spectrum. The resulting offsets are, however, comparably well defined which made us confident to apply this procedure. The described method had no significant impact on the final result at the current level but it might provide a helpful tool in the future to check for potential inter-spectra shifts. The resulting velocities reflect the offsets of the individual spectra to a reference redshift of the H<sub>2</sub> absorber. Of the 11 shifts a mean velocity offset (relative to the assumed  $z_{\text{abs}}$ ) of 46 m s<sup>-1</sup> was computed<sup>2</sup>. This low residual offset verifies the assumed redshift for the absorption system.

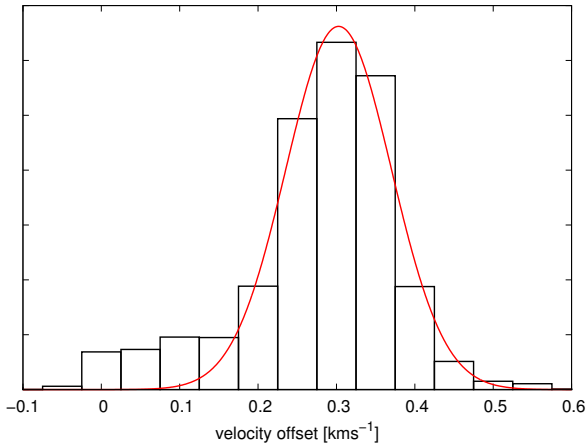


**Fig. 2.** Exemplary bootstrap histogram of the median position of lines in spectrum 8 with respect to  $z = 3.02489817$ . The Gaussian fit corresponds to  $302 \pm 4$  m s<sup>-1</sup> (compare Table 2).

#### 4. Selection of lines and line fitting

For the analysis a total set of 50 H<sub>2</sub> lines are fitted. This preselection is based on earlier line identifications (see Wendt & Molaro 2011) including curve of growth analysis to avoid blends with the Lyman- $\alpha$  forest or other H<sub>2</sub> lines. The separate spectra are

<sup>2</sup> A non-zero mean radial velocity directly reflects a deviation from the assumed absorber redshift.

not coadded in this step since the fitting algorithm works on the different data sets simultaneously. This allows us to omit further rebinning of the data. The fitting code is based on an evolutionary algorithm, which tracks the global minimum via an interactive process of covering the parameter space (see Quast et al. 2005). Each set of fitting parameters is evaluated via  $\chi^2$  in every single spectra. Thus, there is no need to redistribute the flux of each exposure to pixels of equal central wavelengths. Constant velocity offsets, however, potentially influence the shapes of the absorption features as would be the case of coadded spectra. Evolutionary fitting algorithms are less prone to converge in a local minimum rather than find the global minimum. An advantage over Monte Carlo chain methods as applied for the purpose of line fitting in simple cases for example in King et al. (2008) is the drastically reduced need for computer power. Additionally, the principle of evaluating multiple groups of parameters independently allows for consequent parallel computing.

For each set of lines sharing the same rotational level a common column density and a common broadening parameter is fitted with simplified pseudo-Voigt-function profiles. For weak lines a mere Gaussian profile would suffice since natural line broadening has no noticeable impact on the line shapes. In case of QSO 0347-383, only a single component is observed in H<sub>2</sub>. The only free parameter per each individual line is the radial velocity with respect to the absorber redshift. Out of the 50 H<sub>2</sub> lines analyzed, eight were excluded since they showed a comparably large positioning error of more than 300 m s<sup>-1</sup>. This is mostly due to a continuum highly contaminated by the presence of hydrogen absorption in the environment of the affected lines.

We note that our procedure is different from the one followed by King et al. (2008). They fitted numerous additional components in a region of H<sub>2</sub> absorption to narrow down the  $\chi^2$  of the fit to the data.

Figure 3 compares a portion of spectrum used in the analyses by Ivanchik et al. (2005), King et al. (2008), Thompson et al. (2009), and Wendt & Molaro (2011) with the same portion of the new data we are analyzing here. The *solid red* vertical lines mark the H<sub>2</sub> component L4R1 and L4P1 and the *dotted red* lines indicate the 12 additional lines in that region<sup>3</sup>. The *upper* plot corresponds to the data of 2009 and reveals that some of the extra components clearly recreate the flux observed in 2002 but evidently do not correspond to factual properties of the absorber.

In King et al. (2008) the evolution of  $\chi^2$  with an increasing number of additional free lines is the main criterion to fix the total number of components. While that approach clearly reduces the residuals of the fit, it may not reflect the physical properties of the absorber. Though it is likely that the absorber structure is too complex to be represented by a single component, we prefer to integrate the uncertainty of the true nature of the velocity components into the fitting uncertainty rather than 'generating' components to fill up the flux in a poorly known continuum. Higher resolution spectra may verify or falsify some of the decisions on additional components and help to distinguish between apparent precision (lower  $\chi^2$ ) and reached accuracy (better description of the physical conditions of the absorber) or rather the limit on information on the absorber.

#### 5. Results

In Figure 4 the measured radial velocities of the 42 H<sub>2</sub> lines are plotted against the sensitivity towards  $k$  coefficients of the cor-

<sup>3</sup> Their individual positions are extracted from the plot in King et al. (2008).

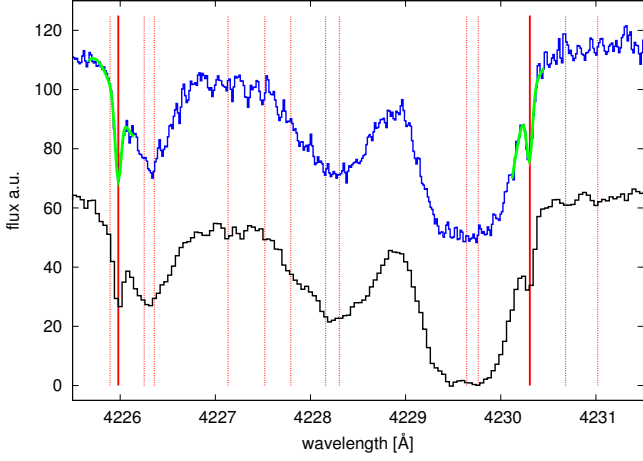


**Fig. 3.** Comparison between the 2009 data (*top graph*) and, with an offset, the original single observation run data of 2002 (9 frames, *bottom*) as used by Ivanchik et al. (2005), King et al. (2008), Thompson et al. (2009), and Wendt & Molaro (2011). The vertical lines indicate the positions of the H<sub>2</sub> component (*solid*) and the 12 additional lines fitted in King et al. (2008). In green the single line fits (L4R1 and L4P1) with their corresponding local continuum polynomial fit from this work. Note, that the fits for the analysis were not carried out on the rebinned and coadded data as shown in this figure.

responding transition. Any correlation therein would indicate a variation of  $\mu$  at  $z=3.025$  with respect to laboratory values. Table 3 lists the broadening parameter and the column density for all the lines from one particular J level fit together and consistently with one N and one b per rotation level.

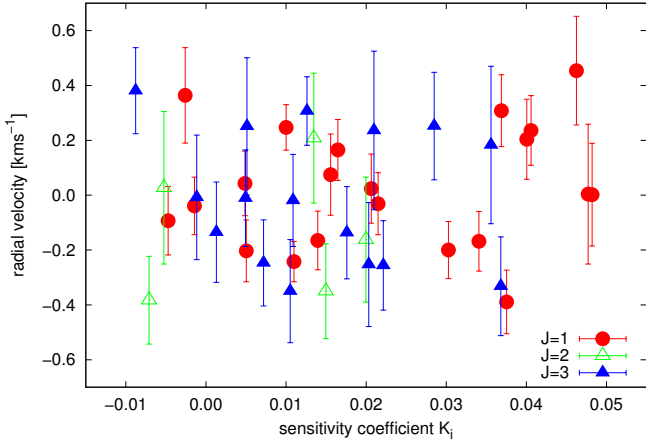


**Fig. 4.** Measured radial velocity vs. sensitivity for all 42 lines. Any correlation would indicate a change in  $\mu$ . The different symbols and colors used correspond to the observed three rotational levels. The errorbars reflect the  $1\sigma$  errors.

The data give no hint towards variation of the proton-to-electron mass ratio in the course of cosmic time. The uncertainties in the line positions of the H<sub>2</sub> features due to the photon noise are estimated by the fitting algorithm. These are shown in the errorbars in Figure 4 and reported in Table 4. The mean error in the line positioning is of  $152\text{ m s}^{-1}$ . Even at first glance the given errorbars in Figure 4 appear to be too small to explain the observed scatter.

Figure 5 shows the same line data as is Figure 4 but lines with similar  $k$  values are binned. For a better overview, errorbars are omitted. The red data points (*crosses*) reflect the radial velocity within a small sensitivity range (given as x-errorbar). The y-errorbars correspond to the standard deviation of the mean value of the scatter within such a bin. The scatter within the bins can not be attributed to possible variations of  $\mu$  since it is present for basically the same sensitivity parameter. The scatter is of the order of  $220\text{ m s}^{-1}$  and thus larger than the positioning error of the individual lines. That is also reflected by a reduced

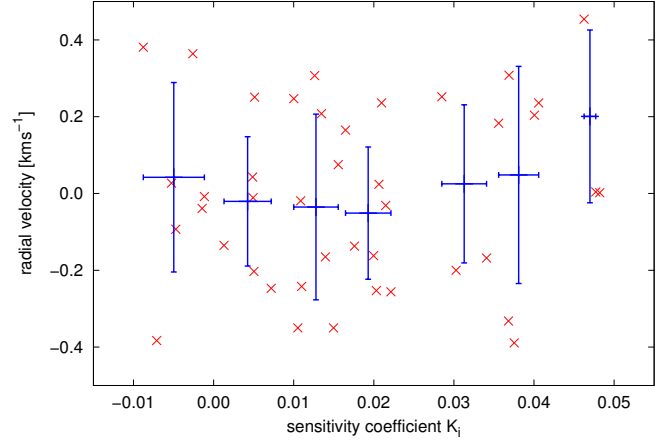


**Fig. 5.** The observed 42 H<sub>2</sub> lines with their corresponding radial velocities. In blue, bins of similar sensitivity are plotted. Blue y-errorbars reflect the standard deviation of radial velocities within an interval (x-errorbar).

$\chi^2$  of 2.7 for a weighted linear fit to the data (corresponding to  $\Delta\mu/\mu = (1.8 \pm 8.2) \times 10^{-6}$  at  $z_{\text{abs}} = 3.025$ ). The true scatter of the data is of the order of  $220\text{ m s}^{-1}$  and constitutes an absolute limit of precision. The above mentioned errors of the fitting procedure require an additional systematic component to explain the observed scatter:

$$\sigma_{\text{obs}} \sim \sqrt{\sigma_{\text{pos}}^2 + \sigma_{\text{sys}}^2}, \quad (3)$$

with  $\sigma_{\text{obs}} = 220\text{ m s}^{-1}$ ,  $\sigma_{\text{pos}} = 152\text{ m s}^{-1}$ , and  $\sigma_{\text{sys}} = 151\text{ m s}^{-1}$ .

A direct linear fit to the unweighted data yields:

$$\Delta\mu/\mu = (4.2 \pm 7.7) \times 10^{-6}. \quad (4)$$

Bootstrap analysis is a robust approach to obtain a linear fit to the data in Figure 4 and estimate an error based on the true scatter of the data. The corresponding bootstrap histogram including Gaussian fit is illustrated in Figure 6. The Gaussian fit gives:

$$\Delta\mu/\mu = (4.3 \pm 7.2) \times 10^{-6}. \quad (5)$$

## 6. Systematics

Any process which influences the measured redshift in dependence with the excitation energy would mimic a variation in  $\mu$  since the transitions from higher excited states naturally show a stronger sensitivity towards changes in  $\mu$  (see Varshalovich & Levshakov 1993). Figure 7 marks the wavelength ranges covered by the different orders of the CCD spectrum. Decreasing

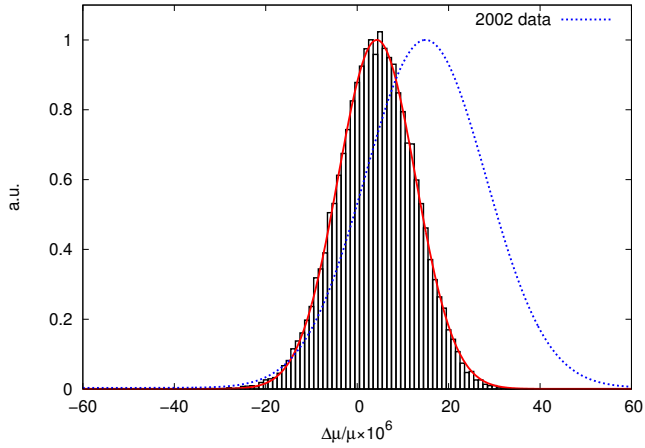


**Fig. 6.** Bootstrap histogram of 50,000 samples based on all 42 lines. The dashed line shows the bootstrap fit of the 2002 data of QSO 0347-383.

wavelengths are plotted rightwards since  $K$  sensitivity factors are increasing almost linearly with decreasing wavelengths and therefore Figure 7 is comparable with Figure 4. This new figure shows no trend but again a rather high scatter within the individual orders can be perceived.

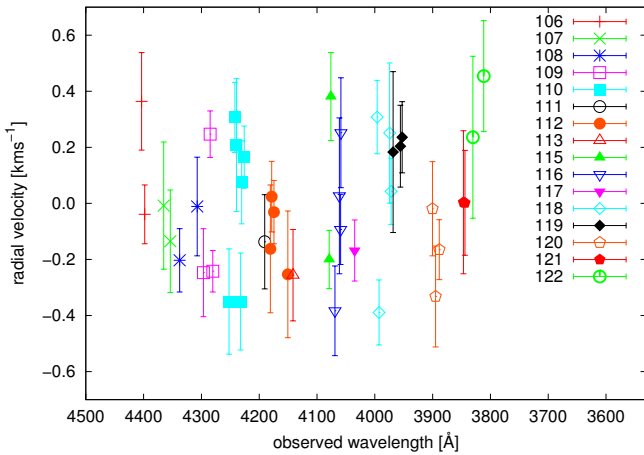


**Fig. 7.** All 42 lines with their radial velocity against the observed wavelength. Different orders are distinguished by colors and symbols.

In the following, we consider a possible correlation of the line position uncertainty and its relative position within an order. Spectral distortions within the spectral orders have been investigated at the Keck/HIRES spectrograph by comparing the ThAr wavelength scale with a second one established from I2-cell observations of a bright quasar by Griest et al. (2010). In the wavelength range  $\sim 5000 - 6200 \text{ \AA}$  covered by the iodine cell absorption they found both absolute offsets which can be as large as  $500 - 1000 \text{ m s}^{-1}$  and an additional saw-tooth distortion pattern with an amplitude of about  $300 \text{ m s}^{-1}$ . The distortions are such that transitions at the order edges appear at different velocities with respect to transitions at the order centers when calibrated with a ThAr exposure. This would introduce relative velocity shifts between different absorption features up to a magnitude the analysis with regard to  $\Delta\mu/\mu$  is sensitive to.

Whitmore et al. (2010) recently repeated the same test for UVES with similar finding though the saw-tooth distortions show slightly reduced peak-to-peak velocity variations of  $\sim 200 \text{ m s}^{-1}$ . The physical explanation for those distortions is not yet known, so it is still to be examined whether the deviations are the same at other wavelengths or depend on the specific exposure.

The available solar atlas can be used to check UVES interorder distortions as suggested in Molaro & Centurion (2011). For this purpose UVES observations of the solar spectrum reflected by the asteroid Iris were taken on Sep 2009 with a resolving power  $R \approx 85000$ .

The differences of the positions in the UVES spectrum and the absolute positions of the solar atlas for 238 solar photospheric lines in the region between 500-530 nm (Orders 121 to 116) are shown in Fig 8. The schematic saw-tooth pattern detected by Whitmore et al. (2010) is also sketched in the figure. The stochastic distribution of the data points does not allow for any conclusion to be drawn about an underlying pattern. The observed dispersion is of  $82 \text{ m s}^{-1}$ . Since the typical error in the measurement of lines in the UVES Iris spectrum is of  $\approx 30 \text{ m s}^{-1}$  and wavelength calibration residuals are of  $25 \text{ m s}^{-1}$ , there is an excess in the observed dispersion which suggests the presence of local deviations in the UVES spectrum. The saw-tooth pattern detected by Whitmore et al. (2010) is not revealed by our test.

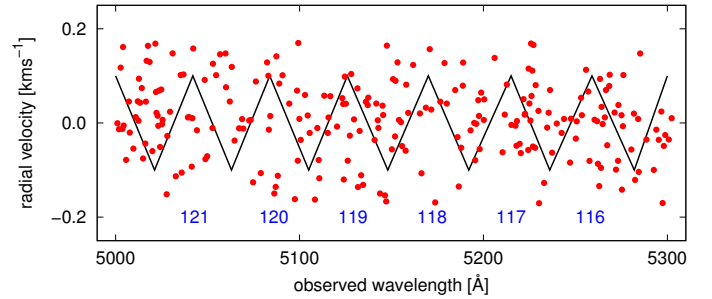


**Fig. 8.** Radial velocity shifts of individual lines Molaro et al. (2011).

Figure 9 sorts the observed lines according to their relative position within their order. The origin of the abscissa reflects the central position within an order. All observed orders are stretched to an identical scale and over-plotted for this purpose. Lines near  $-1/2$  on the X-axis are positioned near the left rim of the order, and so on. The distribution of obtained radial velocities seems to show a certain periodic pattern. The blue curve shows a fitted cosine with an amplitude of  $151 \text{ m s}^{-1}$ . Considering the errorbars of the individual lines, this is no more than a slight indication which supports the presence of local distortions resulting from a non perfect calibration. Systematic errors at the level of few hundred  $\text{m s}^{-1}$  have been revealed also in the UVES data by comparison of relative shifts of lines with comparable response to changes of fundamental constants (Centurion et al. 2009) and Molaro et al (2012). Molaro et al (2012) suggest that these distortions may originate from the block stitching of the CCDs. A CCD device is built-up by means of several sub-unit blocks with typical sizes of 512 pixels. The stitching of the blocks process produces misalignments of the order of few 0.01 of the pixel size in the block conjunctions. The ThAr has not enough lines to follow these imperfections which are therefore flattened in the pixel-to-wavelength conversion by a low order polynomial resulting into the observed spectral distortions.

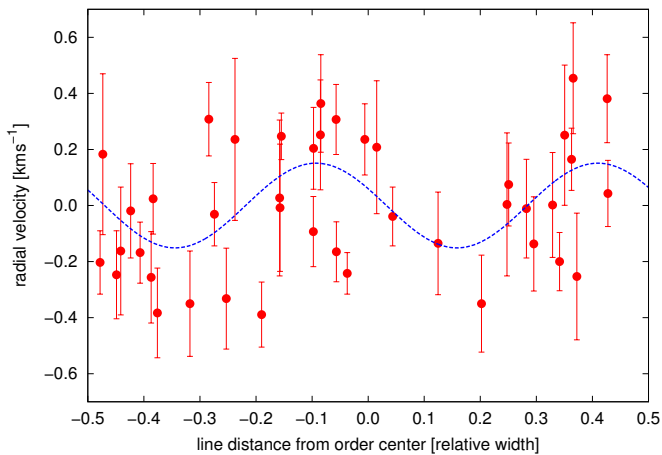


**Fig. 9.** All 42 lines with their radial velocity against their relative position within their order. A cosine fit with an amplitude of  $151 \text{ m s}^{-1}$  is shown in blue.

## 7. Discussion

The result of  $\Delta\mu/\mu = (4.3 \pm 7.2) \times 10^{-6}$  we obtained is consistent with no variation of  $\mu$  between  $z_{\text{abs}} = 3.025$  and  $z = 0$ . The null result is in agreement with recent publications on  $\Delta\mu/\mu$  by King et al. (2011) and Weerdenburg et al. (2011) at  $z_{\text{abs}} = 2.811$  and  $z_{\text{abs}} = 2.059$ , respectively. However, the present work utilizes the line-by-line fitting method (as i.e. in Ivanchik et al. 2005) in contrast to the other works which applied a comprehensive fitting method (CFM). The  $\text{H}_2$  system in the spectrum of QSO 0347-383 has the particular advantage of comprising a single velocity component, which renders observed transitions independent of each other. For absorption systems with two or more closely and not properly resolved velocity components many systematic errors may influence distinct wavelength areas. The CFM fits all  $\text{H}_2$  components along with additional  $\text{H}_I$  lines and handles an artificially applied  $\Delta\mu/\mu$  as free parameter in the fit. The best matching  $\Delta\mu/\mu$  is then derived via the resulting  $\chi^2$  curve. The CFM aims to achieve the lowest possible  $\chi^2_\nu$  via additional velocity components. In this approach the information of individual transitions is lost though since merely the overall quality of the comprehensive model is judged.

In Weerdenburg et al. (2011) the number of velocity components is increased as long as the composite residuals of several selected absorption lines differ from flat noise. The residuals therein do not take into account the known inaccuracy of the estimated flux error (see, i.e., Wendt & Molaro 2011, King et al. 2011).

As pointed out by King et al. (2011), for multi-component structures with overlapping velocity components the errors in the line centroids are heavily correlated and a simple  $\chi^2$  regression is no longer valid. The same principle applies for co-added spectra with relative velocity shifts. The required rebinning of the contributing data sets implements further autocorrelation of the individual ‘pixels’.

The uncertainties of the oscillator strengths  $f_i$  that are stated to be up to 50% (Weerdenburg et al. 2011) might further affect the criteria for additional velocity components. The method of CFM was applied for QSO 0347-383 by King et al. (2008). Section 4 and in particular Figure 3 reveal some of the mentioned difficulties. The approach to fit individual lines with common physical properties which was applied here allows us to carry out an error analysis which reproduces the impact of dif-

ferential shifts within the spectral orders. This yields a higher transparency of the error-budget for individual lines but at the possible cost of larger scatter resulting in a slightly larger error-estimate. For the small number of  $\text{H}_2$  lines observed in the spectrum of QSO 0347-383 we prefer the method applied in this work. The immediate advantage is that we are not forced to estimate the different systematic errors based on assumptions. Instead the true limiting error can be gathered directly from the data distribution and we are further able to attribute it to different sources.

The new set of UVES observations of QSO 0347-383 this analysis is based has been taken with special care aimed to improve the measurement of  $\Delta\mu/\mu$  in a robust manner. In particular the observations have been taken with higher resolution, a  $1 \times 1$  binning and calibration lamp spectra in direct combination with the main exposures. These boost the precision of the analysis roughly by a factor two with comparison with Wendt et al. (2008). We have shown that at the current level, calibration issues become the dominant source of error. In addition to positioning errors, which are related to the signal-to-noise-ratio of the data, we observe for the first time inter order distortions which seem to be of the same order of magnitude of the uncertainties in the line positions. The conclusion is that we do not detect change in the value of  $\mu$  to 1 part in  $10^5$  over a time span of 11.5 Gyr, which is approximately 80% of the age of the universe.

High resolution data and attached calibration spectra are the key to understanding and handling the systematics which limit the precision of  $\Delta\mu/\mu$  measurements. It is important to fully control the analysis of individual absorption systems and to minimize the errors involved wherever possible before extending the  $\Delta\mu/\mu$  analysis to multiple systems. Different characteristics of individual absorbers tend to get lost while not all errors of the measurements are likely to average out.

Until new ways of wavelength calibration such as optical laser frequency combs (see i.e. Steinmetz et al. 2008) are installed for large optics, the data at hand is of the best quality available. High resolution VLT-data with special care regarding the calibration frames allows for the best precision that can be reached nowadays. In the context of  $\Delta\mu/\mu$  measurements, optical spectra of  $\text{H}_2$  at high redshifts are still of high importance to complement high precision determinations of  $\Delta\mu/\mu$  in the local universe via observations in the radio regime.

*Acknowledgements.* We are thankful for helpful discussions on this topic with S.A. Levshakov and D. Reimers.

## References

- Bagdonaite, J., Murphy, M. T., Kaper, L., Ubachs, W. 2012, arXiv:1112.0428v1
- Blatt, S. and Ludlow, A. D. and Campbell, G. K., et al. 2008, Phys. Rev. Lett., 100, 14
- Centurión, M. and Molaro, P. and Levshakov, S. 2009, ArXiv 0910.4842
- Edlén, B. 1966, Metrologia, 2, 71
- Flambaum, V. V. and Leinweber, D. B. and Thomas, A. W. and Young, R. D. 2004, Phys. Rev. D, 69
- Flambaum, V. V. & Kozlov, M. G. 2007, Phys. Rev. Lett., 98, 24
- Fritzsch, H. 2009, arXiv:0902.2989
- Griest, K. and Whitmore, J. B., Wolfe, A. M., et al. 2010, ApJ, 708, 158
- Ivanchik, A. and Petitjean, P. and Varshalovich, D., et al. 2005, ApJ, 440, 45
- Kanekar, N. and Chengalur, J. N. and Ghosh, T. 2010, ApJ, 716, 23
- Kanekar, N. and Prochaska, J. X. and Ellison, S. L. and Chengalur, J. N., 2010, ApJ, 712, 148
- Kaufer, A. and D’Odorico, S. and Kaper, et al. 2004, UVES User manual
- Khatri, R. & Wandelt, B. D., 2007, Phys. Rev. Lett., 98, 11
- King, J. A. and Webb, J. K. and Murphy, M. T. and Carswell, R. F. 2008, Phys. Rev. Lett., 101

- King, J. A. and Murphy, M. T. and Ubachs, W. and Webb, J. K. 2011, MNRAS, 417, 3010
- Levshakov, S. A. and Dessauges-Zavadsky, M. and D'Odorico, S. and Molaro, P. 2002, MNRAS, 333, 373
- Levshakov, S. A. and Dessauges-Zavadsky, M. and D'Odorico, S. and Molaro, P. 2002, ApJ, 565, 696
- Levshakov, S. A. and Molaro, P. and Lapinov, A. V. et al. 2010, A&A, 512, 44
- Levshakov, S. A. and Lapinov, A. V. and Henkel, C., et al. 2010, A&A, 524, 32
- Levshakov, S. A. and Kozlov, M. G. and Reimers, D. 2011, ApJ, 738, 26
- Lybanon, M. 1984, AJP, 52, 22
- Mohr, P.J. & Taylor, B.N. 2000, Rev.Mod.Phys. 72, 351
- Malec, A. L. and Buning, R. and Murphy, M., et al. 2010, MNRAS, 403, 1541
- Meshkov, V. V., Stolyarov, A. V., Ivanchik, A. V., Varshalovich, D. A. 2006, JETPL, 83, 303
- Molaro, P. and Levshakov, S. A. and Monai, S., et al. 2008, A&A, 481, 559
- Molaro, P. and Reimers, D. and Agafonova, I. I. and Levshakov, S. A. 2008, EPJ, 163, 173
- Molaro, P. and Centurión, M. 2011, A&A, 525, 74
- Molaro, P. Centurión, M. et al 2012, in preparation
- Murphy, M. T. and Tzanavaris, P. and Webb, J. K. and Lovis, C. 2007, MNRAS, 378, 221-230
- Murphy, M. T. and Webb, J. K. and Flambaum, V. V., et al. 2008, MNRAS, 384, 1053
- Potekhin, A. Y., Ivanchik, A. V., Varshalovich, D. A., et al. 1998, ApJ, 505, 523
- Quast, R. and Baade, R. and Reimers, D. 2005, ApJ, 431, 1167
- Reinhold, E. and Buning, R. and Hollenstein, U., et al. 2006, Phys. Rev. Lett., 96, 15
- Steinmetz, T. and Wilken, T. and Araujo-Hauck, et al. 2008, Science, 321, 1335
- Thompson, R. I. 1975, Astrophys. Lett., 16, 3
- Thompson, R. I. and Bechtold, J. and Black, J. H., et al. 2009, ApJ, 703, 2
- Thompson, R. I. and Bechtold, J. and Black, J. H. and Martins, C. J. A. P. 2009, New A, 14, 379
- Ubachs, W. and Buning, R. and Eikema, K. S. E. and Reinhold, E. 2007, J. Molec. Spec., 241, 155
- Varshalovich, D. A. and Levshakov, S. A. 1993, JETP, 58, 231
- Varshalovich, D. A. and Potekhin, A. Y. 1995, Space Sci. Rev., 74, 259
- Wendt, M. & Reimers, D. 2008, EPJ, 163, 197
- Wendt, M. & Molaro, P. 2011, A&A529, 96
- van Weerdenburg, F. and Murphy, M. T. and Malec, A. L. and Kaper, L. and Ubachs, W. 2011, Phys. Rev. Lett., 106, 18
- Whitmore, J. B. and Murphy, M. T. and Griest, K. 2010, ApJ, 723, 89



**Table 3.** Line parameters for the observed three rotational levels of  $H_2$ .

J	b [km s <sup>-1</sup> ]	logN
1	1.34 ± 0.04	14.36 ± 0.02
2	1.39 ± 0.32	13.72 ± 0.02
3	2.02 ± 0.05	13.91 ± 0.01

**Table 4.** List of 42  $H_2$  lines fitted in QSO 0347-383. Radial velocities given relative to a redshift of  $z = 3.02489817$ .

Line ID	Lab. wavelength [Å]	Obs. wavelength [Å]	Pos. error [Å]	Velocity [km s <sup>-1</sup> ]	Vel. error [km s <sup>-1</sup> ]	<i>K</i> factor
L1P1	1094.0519	4403.4530	0.0026	0.364	0.174	-0.003
L1R1	1092.7324	4398.1360	0.0015	-0.039	0.105	-0.001
L2R1	1077.6989	4337.6252	0.0016	-0.203	0.113	0.005
L3P1	1064.6053	4284.9315	0.0012	0.247	0.083	0.010
L3R1	1063.4601	4280.3151	0.0011	-0.242	0.074	0.011
L4P1	1051.0325	4230.2996	0.0021	0.075	0.148	0.016
L4R1	1049.9597	4225.9832	0.0016	0.165	0.111	0.016
L5P1	1038.1570	4178.4767	0.0018	0.024	0.126	0.021
L5R1	1037.1498	4174.4220	0.0016	-0.031	0.113	0.021
L7R1	1013.4369	4078.9777	0.0014	-0.200	0.104	0.030
L8R1	1002.4520	4034.7650	0.0015	-0.168	0.109	0.034
L9P1	992.8096	3995.9617	0.0017	0.308	0.131	0.037
L9R1	992.0163	3992.7595	0.0015	-0.389	0.116	0.038
L10P1	982.8353	3955.8147	0.0019	0.204	0.146	0.040
L10R1	982.0742	3952.7519	0.0017	0.236	0.127	0.041
L13P1	955.7082	3846.6281	0.0033	0.004	0.255	0.048
L13R1	955.0658	3844.0424	0.0024	0.002	0.187	0.048
L14R1	946.9804	3811.5054	0.0025	0.454	0.198	0.046
W0R1	1008.4982	4059.1012	0.0017	-0.093	0.125	-0.005
W1Q1	986.7980	3971.7622	0.0016	0.043	0.118	0.005
W2Q1	966.0961	3888.4364	0.0014	-0.165	0.107	0.014
L4P2	1053.2842	4239.3646	0.0034	0.208	0.237	0.013
L4R2	1051.4985	4232.1695	0.0024	-0.350	0.173	0.015
L5R2	1038.6902	4180.6199	0.0032	-0.162	0.228	0.020
W0Q2	1010.9385	4068.9194	0.0022	-0.383	0.160	-0.007
W0R2	1009.0250	4061.2231	0.0038	0.027	0.278	-0.005
L2P3	1084.5603	4365.2445	0.0033	-0.008	0.227	-0.001
L2R3	1081.7113	4353.7758	0.0027	-0.135	0.183	0.001
L3P3	1070.1408	4307.2077	0.0025	-0.011	0.176	0.005
L3R3	1067.4786	4296.4891	0.0022	-0.247	0.157	0.007
L4P3	1056.4714	4252.1847	0.0027	-0.350	0.188	0.011
L4R3	1053.9761	4242.1506	0.0018	0.307	0.125	0.013
L5R3	1041.1588	4190.5564	0.0024	-0.137	0.168	0.018
L6P3	1031.1927	4150.4420	0.0031	-0.253	0.226	0.020
L6R3	1028.9866	4141.5628	0.0023	-0.256	0.163	0.022
L8P3	1008.3861	4058.6547	0.0027	0.252	0.196	0.028
L10R3	985.9628	3968.4022	0.0038	0.183	0.287	0.036
L12R3	967.6770	3894.7970	0.0023	-0.332	0.180	0.037
W0Q3	1012.6796	4075.9375	0.0021	0.381	0.157	-0.009
W1R3	987.4487	3974.3837	0.0033	0.251	0.250	0.005
W2Q3	969.0493	3900.3246	0.0022	-0.019	0.168	0.011
W3P3	951.6718	3830.3853	0.0037	0.236	0.289	0.021